The Astrophysical Journal, 687:668–677, 2008 November 1

ARE THERE FIELD-FREE GAPS NEAR $\tau = 1$ IN SUNSPOT PENUMBRAE?

J. M. Borrero
High Altitude Observatory (NCAR), 3080 Center Green Drive, CG-1, Boulder, CO 80301; borrero@ucar.edu

and

S. K. Solanki
Max-Planck-Institut für Sonnensystemforschung, Max-Planck-Strasse 2, 37191 Katlenburg-Lindau, Germany; solanki@mps.mpg.de
Received 2008 March 8; accepted 2008 June 18

ABSTRACT

The vertical stratification of the magnetic field strength in sunspot penumbrae is investigated by means of spectropolarimetric observations at high spatial resolution from the *Hinode* spacecraft. Assuming that the magnetic field changes linearly with optical depth we find that, in those regions where the magnetic field is more inclined and the Evershed flow is strongest (penumbral intraspines), the magnetic field can either increase or decrease with depth. Allowing more degrees of freedom to the magnetic field stratification reveals that the magnetic field initially decreases from $\log \tau_5 = -3$ until $\log \tau_5 \simeq -1.0$, but increases again below that. The presence of strong magnetic fields near the continuum is at odds with the existence of regions void of magnetic fields at, or right below, the $\tau_5 = 1$ level in the penumbra. However, they are compatible with the presence of a horizontal flux-tube-like field embedded in a magnetic atmosphere.

Subject headings: polarization — Sun: magnetic fields — sunspots

1. INTRODUCTION

It is now widely accepted that the horizontal structure of the sunspot penumbra is composed of two magnetic components (Solanki 2003; Bellot Rubio 2003). One of them possesses a somewhat inclined ($\simeq 40^\circ$–50° with respect to the vertical direction to the solar surface) and strong ($\sim$2000 G) magnetic field, whereas the other is characterized by a weaker and more horizontal one (Lites et al. 1993; Rüedi et al. 1998; Bellot Rubio et al. 2004; Borrero et al. 2004, 2005). Traditionally, these two magnetic components have been identified with a horizontal flux tube, that carries the Evershed flow, and is embedded in a more vertical background magnetic field: *uncombed* model (Solanki & Montavon 1993; Schlichenmaier et al. 1998; Borrero 2007). Recently, this view has been challenged by Spruit & Scharmer (2006) and Scharmer & Spruit (2006), who propose instead that the penumbra is formed by magnetic field-free plumes (connected to the underlying convection zone) that pierce the penumbral magnetic field from beneath. This is the so-called *gappy* penumbral model.

So long as these two different magnetic structures (weak/horizontal and strong/vertical) have remained spatially (horizontally) unresolved, distinguishing between the uncombed and gappy penumbral scenarios has not been possible. However, with the new spectropolarimeter on board the Japanese spacecraft *Hinode* (Kosugi et al. 2007; Shimizu et al. 2008) it is now possible to obtain high spatial resolution ($\simeq 0.32''$) observations of the sunspot penumbra. This could be sufficient to distinguish between the uncombed and gappy models, since they both postulate the existence of flux tubes or field-free gaps that are about 200–300 km in diameter (Martínez Pillet 2000; Spruit & Scharmer 2006). This feature is particularly interesting, because the uncombed and gappy models predict very different vertical stratifications in the magnetic field strength across the weak/horizontal magnetic field component, which is identified with an embedded flux tube in the uncombed model, but with a field-free gap in the gappy model. In the latter, the magnetic field decreases monotonically with depth, whereas the former possesses a magnetic field that decreases with depth only initially; since once the boundary of the flux tube is reached, the magnetic field can either decrease or increase depending on the strength of the magnetic field inside the tube.

In this paper we will focus on obtaining the vertical stratification of the magnetic field for penumbral filaments (where the magnetic field is more horizontal and weaker) using high spatial resolution spectropolarimetric observations from *Hinode*, in order to establish which penumbral model is more realistic. The observations are described in § 2. Section 3 describes our data analysis and results from our inversion technique. Section 4 compares our findings with the predictions made by the uncombed and gappy penumbral models. In § 5 we make a thorough investigation of the effects of the scattered light. Finally, § 6 summarizes our findings.

2. OBSERVATIONS

On 2007 May 3, between 10:15 and 11:40 UT, AR 10953 was mapped using the spectropolarimeter of the Solar Optical Telescope on board the *Hinode* spacecraft (Lites et al. 2001). The active region was located at a heliocentric angle of $\theta = 19.2^\circ$. It was scanned in a thousand steps, with a step width of $0.148''$ and a slit width of $0.158''$. The spectropolarimeter recorded the full Stokes vector (I, Q, U, and V) of the pair of neutral iron lines at 630 nm with a spectral sampling of 21.53 mÅ. The integration time was 4.8 s, resulting in an approximate noise level of 1.2×10^{-3} (in units of the normalized continuum intensity). In the absence of the telluric oxygen lines we proceeded with two different wavelength calibration methods that were cross-checked for consistency. The first method was obtained by matching the average quiet-Sun profile with the Fourier transform spectrometer (FTS) spectrum, whereas the second calibration assumes that the average umbral profile exhibits no velocities.

A map of the continuum intensity at 630 nm of the scanned region is shown in Figure 1. The white arrow indicates the direction of the center of the solar disk. The penumbra on the center side is heavily distorted and therefore left out of our analysis. On

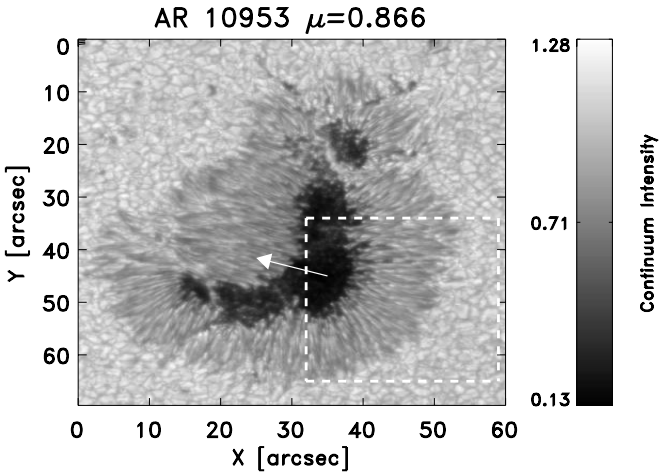

FIG. 1.—Continuum intensity map at 630 nm of AR 10953. This sunspot was observed using *Hinode*'s spectropolarimeter on 2007 May 3, at a heliocentric angle of $\theta = 19°$. The white arrow points toward the center of the solar disk. The white rectangle limits the region chosen for our study. It lies on the limb side around the line of symmetry.

the limb side the penumbra is more uniform, with radially aligned filaments. The region enclosed by the white rectangle has been chosen for our study. This sunspot has negative polarity (magnetic field in the umbra points toward the solar interior); however, the results presented hereafter are shown, in order to facilitate the interpretation, as if the sunspot had positive polarity.

3. DATA ANALYSIS AND RESULTS

We have applied the SIR inversion code (Ruiz Cobo & Del Toro Iniesta 1992) to our spectropolarimetric observations to retrieve the physical properties of the solar atmosphere. This code allows all relevant physical parameters to be a generic function of the optical depth: $B(\tau), \gamma(\tau), \phi(\tau), V_{\rm los}(\tau)$, etc. In addition, a depth-dependent temperature stratification $T(\tau)$ models the atmospheric thermodynamics under local thermodynamic equilibrium (LTE) conditions. SIR retrieves the values of the parameters at a number of optical depth points called *nodes*. The final stratification is obtained by interpolating splines across those nodes. Note, however, that SIR employs equivalent response functions (Del Toro Iniesta 2003), which ensures sensitivity to the atmospheric layers located between nodes. Each node represents a free parameter in the inversion. In our investigation we will employ increasingly complex models (i.e., more free parameters) according to the amount of information we hope to extract from the profiles.

Given the high spatial resolution of *Hinode*'s observations, we will consider only one magnetic component. A nonmagnetic component is also considered to account for the scattered light. In this section, the scattered light profile is obtained by averaging the intensity profiles of those pixels with polarization signals below the noise level (quiet-Sun granulation around the sunspot). The same scattered light profile is used in the inversion of all pixels. In § 5 we make a thorough analysis of the effects that different treatments for the scattered light have on our results. Note that using one single magnetic component is equivalent to assuming that the penumbral structure is horizontally resolved. This is clearly not the case if we look into continuum images at even higher spatial resolution (Scharmer et al. 2002). However, our assumption would still be valid if the (unresolved) variations of the magnetic field inside the weak/horizontal magnetic component are much smaller than the differences between the weak/horizontal and strong/vertical components. Since the former remain unresolved, we cannot assess the validity of this assumption. This question should be addressed as better spectropolarimetric observations become available.

3.1. *One-Node Inversion and Intraspine Selection*

In order to locate the intraspinal pixels we have carried out a first inversion where all physical parameters, with the exception of the temperature, are constant with optical depth. We therefore have one single node for $B(\tau), \gamma(\tau), \phi(\tau), V_{\rm los}(\tau)$. To account for unresolved velocity fields, we also consider depth-independent micro- and macroturbulent velocities: $V_{\rm mic}$ and $V_{\rm mac}$. Another free parameter, $\alpha_{\rm qs}$, represents the fraction of the observed intensity, Stokes I, that corresponds to scattered light. Finally, three nodes are given to the temperature $T(\tau)$. In total, this first inversion has 10 free parameters. Since B, γ, ϕ and $V_{\rm los}$ are constant with optical depth, the retrieved values indicate some kind of average over the region where the spectral lines are formed. Westendorp Plaza et al. (1998, 2001) studied this issue in detail and found that the largest contribution for this pair of Fe I lines (§ 2) comes from $\log \tau_5 \simeq -1.5$.

Figure 2 displays the resulting values for the line-of-sight velocity and magnetic field vector in the selected box in Figure 1. Regions of weak, $B < 1300$ G, and highly inclined, $\gamma > 80°$, magnetic field can be clearly distinguished in this figure. They are also characterized by the presence of large redshifted velocities (Evershed flow). These are the so-called penumbral intraspines, and therefore the most likely locations where field-free gaps or horizontal flux tubes can be found. Also visible are structures characterized by a stronger and more vertical magnetic field, as well as by a strongly reduced Evershed flow. These are usually referred to as spines. Spines and intraspines are also seen at moderate ($\sim 1''$) spatial resolution (Lites et al. 1993; Stanchfield et al. 1997; Mathew et al. 2003), but the associated changes in their properties (field strength, inclination, etc.) are larger if observed at high spatial resolution (Bello González et al. 2005; Langhans et al. 2005). Bellot Rubio et al. (2004) interprets this result as a consequence of these structures not being spatially resolved at $1''$ resolution. As demonstrated by Borrero et al. (2008), they are indeed horizontally resolved in *Hinode* observations ($0.32''$).

In Figure 2 we also indicate with black and white dots a large number (total of 7520) of intraspinal pixels. They have been found as those satisfying the following conditions: $B > 700$ G and $V_{\rm los} \in [1.0, 3.0]$ km s^{-1}. Since the main difference between spines and intraspines is the presence of a strong Evershed flow, we use $V_{\rm los}$ to distinguish among them. However, we do not consider the few pixels where $V_{\rm los} > 3$ km s^{-1}, since they usually present extremely abnormal Stokes V profiles, usually a sign of the existence of horizontally unresolved structure. We do not constrain the values of the magnetic field inclination and strength (here we use only a lower limit to avoid taking pixels outside the visible boundary of the sunspot) because the magnetic properties of the spines in the outer penumbra are very similar to those of the intraspines in the inner penumbra. The final selected pixels represent about 39% of all penumbral pixels in Figure 2. Note that they are mostly located in the middle and outer penumbra: $r/R_s > 0.5$ (R_s being the sunspot radius; the umbral-penumbral boundary is located at $r/R_s > 0.25$). Note also that, even though we have not constrained the values of the magnetic field strength and inclination, all intraspinal pixels are located in regions where the magnetic field is highly inclined and weak.

3.2. *Two-Node Inversion of Individual Profiles*

In order to investigate the depth variation of the physical parameters in intraspines, we performed a renewed inversion of the

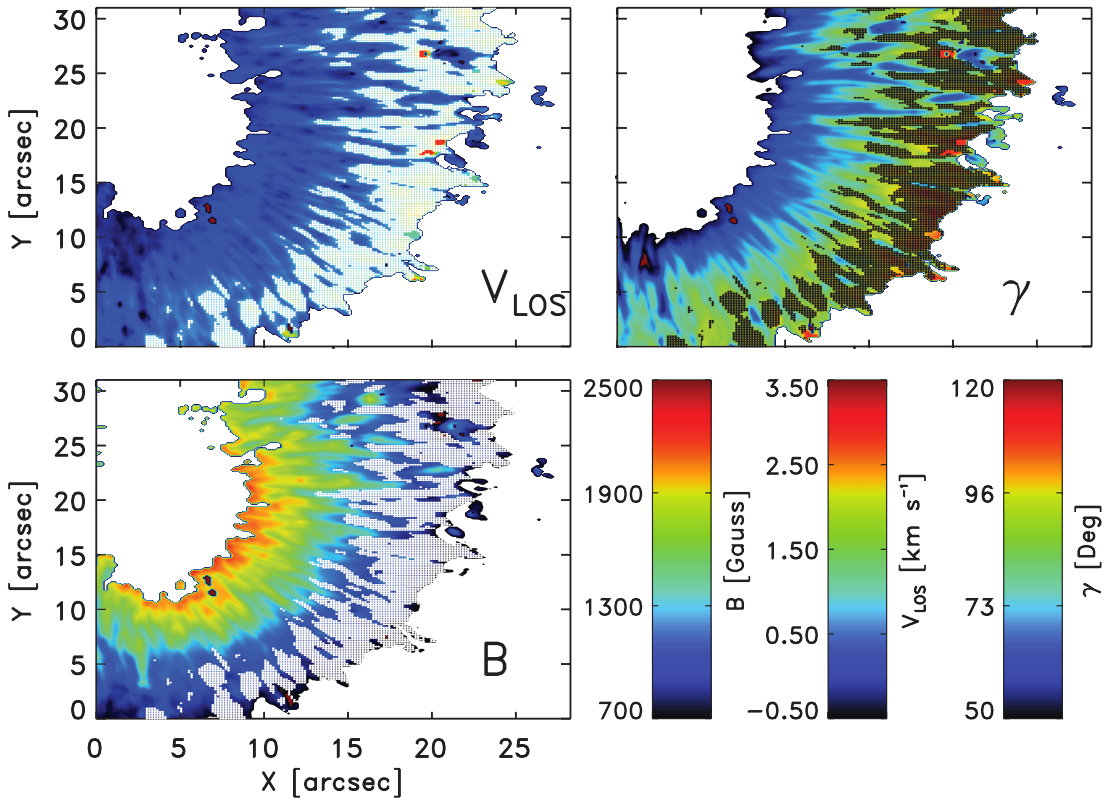

FIG. 2.—Results from the inversion of the region limited by the square box in Fig. 1. The inversion was performed assuming that B, γ, ϕ, and $V_{\rm los}$ are constant with optical depth. The magnetic field strength is displayed in the lower left panel, inclination (*upper right*), and line-of-sight velocity (*upper left*). The white and black dots correspond to those pixels where the location of horizontal flux tubes or field-free gaps are suspected (see text for details). There are 7520 of them: 39% of all penumbral pixels in this figure.

pixels selected in Figure 2, where we now allow for two nodes in $B(\tau)$, $\gamma(\tau)$, $\phi(\tau)$, and $V_{\rm los}(\tau)$ (linear variations with optical depth). The total number of free parameters is now 14. Results from this new inversion are presented in Figure 3: $T(\tau)$ (*upper left*), $V_{\rm los}(\tau)$ (*upper right*), $B(\tau)$ (*lower left*), and $\gamma(\tau)$ (*lower right*). All inverted pixels display similar stratifications of $V_{\rm los}(\tau)$ and $\gamma(\tau)$: both increase monotonically with optical depth: $\partial V_{\rm los}/\partial\tau, \partial\gamma/\partial\tau > 0$. The magnetic field strength $B(\tau)$, however, can either increase (in 66% of inverted pixels: 4971) or decrease (34%; 2249 pixels) with optical depth. In either case, the retrieved gradient is relatively small: $|dB/dz| \leq 1.5$ G km^{-1}. An important feature to note is that pixels displaying a decreasing magnetic field toward deeper layers, $dB/d\tau < 0$, are mostly located in the inner penumbra, whereas pixels showing $dB/d\tau > 0$ are mostly found in the outer penumbra (see Fig. 4).

3.3. *Four-Node Inversion of Individual Profiles*

We now perform a more complex inversion of the same pixels as in § 3.2. In this case we allow for four nodes in $B(\tau)$, $\gamma(\tau)$, $\phi(\tau)$, and $V_{\rm los}(\tau)$. These nodes are located at optical depth positions: $\log_{\tau_5} = [-3.2, -1.8, -0.4, 1]$. In total, this new inversion has 22 free parameters. Figure 5 shows the results from the four-node inversion of the 7250 intraspinal pixels selected in § 3.1. The stratifications are very similar to those already obtained through the two-node inversion (see Fig. 3). The larger scatter (pixel-to-pixel variations) in the four-node inversion is due to the larger amount of free parameters, which are more weakly constrained by the observations.

Since now we allow for four nodes to the stratification of the magnetic field strength, it is not easy to classify our results between those where the magnetic field increases or decreases with optical depth. To showcase the differences between the possible stratifications, we have taken separately those pixels that, in the two-node inversion, showed $dB/d\tau < 0$ (family 1) or $dB/d\tau > 0$ (family 2), and obtained the averaged stratification for the two- and four-node inversion. Results for family 1 and 2 are presented in Figures 6 and 7, respectively.

Interestingly, the magnetic field strength, which in the two-node inversion showed different gradients, now shows an initial decrease up to $\log\tau_5 \simeq -1$ (approximately 100 km above the continuum level), where it starts to increase again toward deep layers. This happens for both families of magnetic structures, and thus could indicate that they are indeed closely related. A closer look reveals that both families possess a similar magnetic field strength in deep layers: $B(\tau = 1) \simeq 1250$ G, but slightly different higher up: $B(\tau = 10^{-3}) \simeq 1200$ G (family 1; Fig. 6) and $B(\tau = 10^{-3}) \simeq 900$ G (family 2; Fig. 7). This effect explains why the two-node inversion (§ 3.2) retrieves different overall gradients for the magnetic field strength: it is due to a large variation in the magnetic field at around $\tau_5 \simeq 10^{-3}$, since the magnetic field deeper down is basically the same in both cases.

To further confirm these results we have repeated our four-node inversion with the nodes located at slightly different positions. SIR always places two nodes at the uppermost and deepest τ-locations of the discretized atmosphere, while spreading the rest equidistantly in between. Therefore, to keep the same number of nodes and, at the same time, change their τ-positions we must change the initial and last τ-points of the atmosphere. In our first set of inversions the atmosphere is discretized between $\log\tau_5 = [-3.2, 1]$. Changing this to $\log\tau_5 = [-3.0, 1.2]$ and $\log\tau_5 = [-3.7, 0.5]$

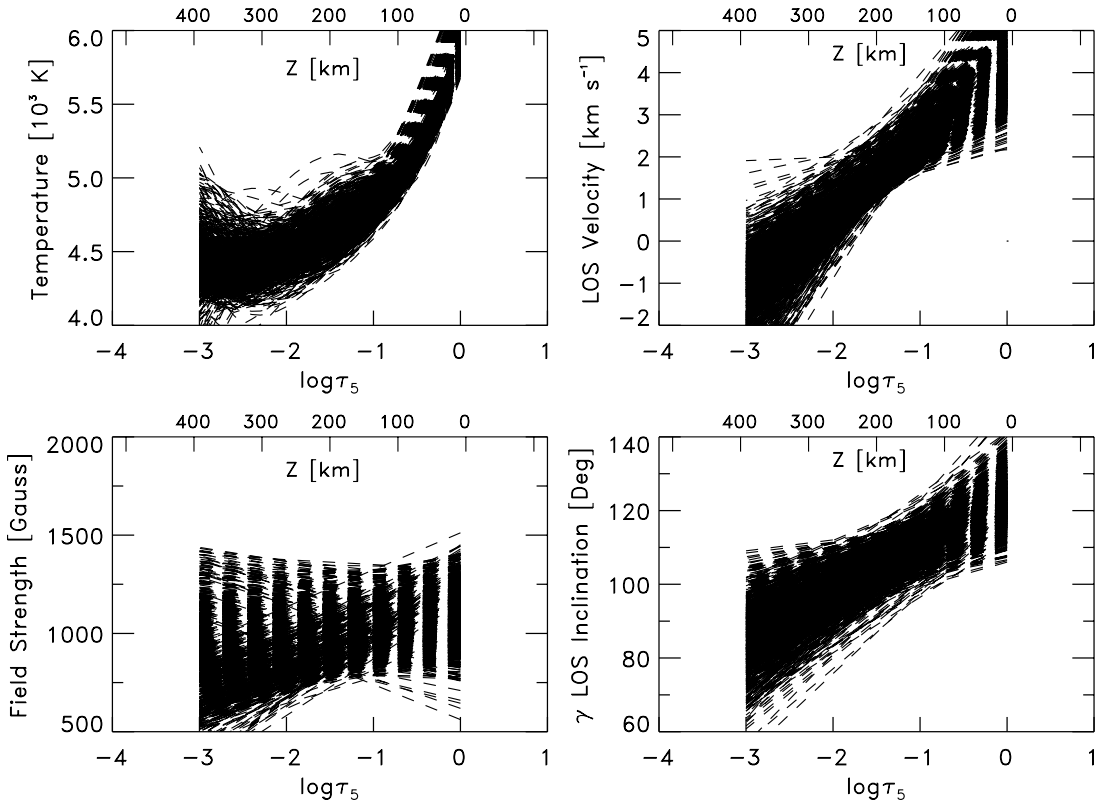

FIG. 3.—Temperature (*upper left*), line-of-sight velocity (*upper right*), magnetic field strength (*lower left*), and magnetic field zenith angle (*lower right*) as a function of the optical depth log τ_5, obtained from the two-node inversion of the intraspinal pixels selected in Fig. 2. Approximate height scale, Z, computed assuming vertical hydrostatic equilibrium, is also indicated.

would position the four nodes at [−3.0, −1.6, −0.2, 1.2] and [−3.7, −2.3, −0.9, 0.5], respectively. We have inverted all pixels again in these two cases and confirmed that our results (Figs. 5–7) do not change. This is due to the use that SIR makes of equivalent response functions (see § 3).

4. DISCUSSION

If we consider a ray passing through the center of an intraspine, the gappy and uncombed penumbral models predict a very similar stratification of the magnetic field strength above the field-free gap or flux tube, but very different ones inside them. Figure 8 illustrates some possible stratifications predicted by these two models, where the upper boundary of the field-free gap and flux tube is located at $z = 0$. Above $z = 0$ they both share the same stratification for the surrounding magnetic atmosphere. Here we present two examples, one where the surrounding magnetic field is weak: $B_{\rm surr} = 1000$ (*dashed line*; meant to represent the outer penumbra, $r/R_s = 0.8$), and another case where the surrounding field is stronger: $B_{\rm surr} = 1500$ (*solid line*; meant to represent to inner penumbra, $r/R_s = 0.4$). Note that the magnetic field strength in the surrounding atmosphere decreases toward deeper layers. This is due to the fact that the vertical component of the surrounding field must vanish (or nearly vanish in the case of a cusp-shaped boundary) at the flux tube's or gap's boundary. These two examples are actual solutions of analytical models (Fig. 5 in Spruit & Scharmer 2006; Fig. 3 in Scharmer & Spruit 2006; see also eqs. [33]–[34] in Borrero 2007). Below the boundary of the flux tube or field-free gap, $z = 0$, both models predict a very different situation. In the case of the gappy penumbra this region is void of magnetic fields: $B_{\rm gap} \simeq 0$ (*open circles*). In contrast, the uncombed model assumes the existence of a flux tube where the magnetic field is strong: $B_{\rm tube} = 1250$ G (*filled circles*).

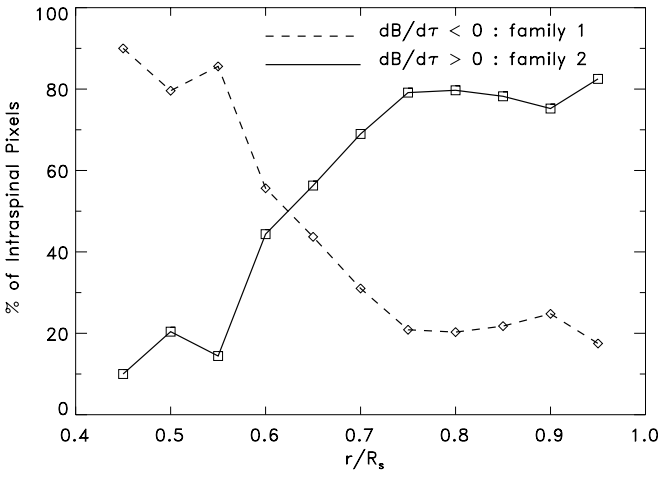

FIG. 4.—Percentage of the total selected pixels that, at each radial distance from sunspot center, show a magnetic field that increases ($dB/d\tau > 0$; *solid line*) or decreases ($dB/d\tau > 0$; *dashed line*) toward the solar interior.

If we compare Figure 8 with our two-node inversion (Fig. 3) of intraspinal pixels we find that, on one hand, the gappy penumbral model can only explain the slowly decreasing magnetic field, observed for 34% of intraspinal pixels (family 1), if the $\tau_5 = 1$ level is formed above the gap's boundary; otherwise, a much more sudden drop would be observed (open circles in Fig. 8). On the other hand, this model does not offer any explanation for the 66% of the intraspinal pixels that present an increasing magnetic field strength toward deeper layers (family 2). However, the uncombed penumbral model can explain both observed situations. It all depends on the strength of the flux tube's magnetic

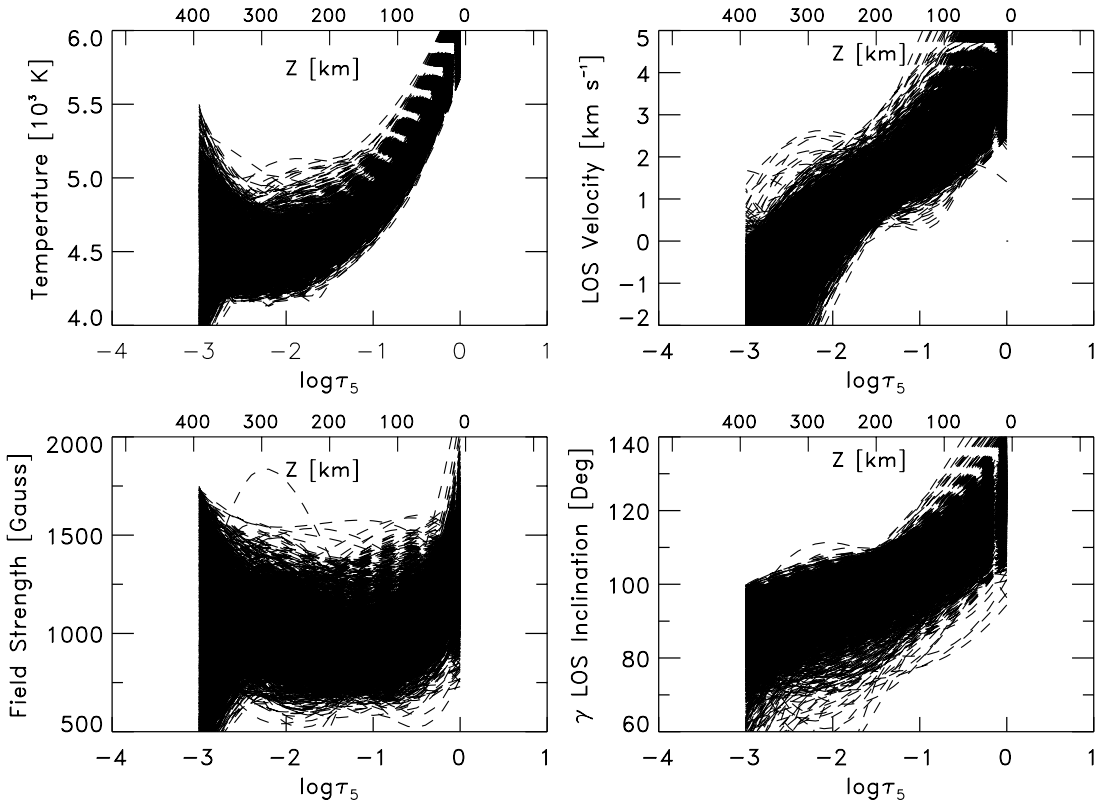

FIG. 5.—Same as Fig. 3, but for the four-node inversion.

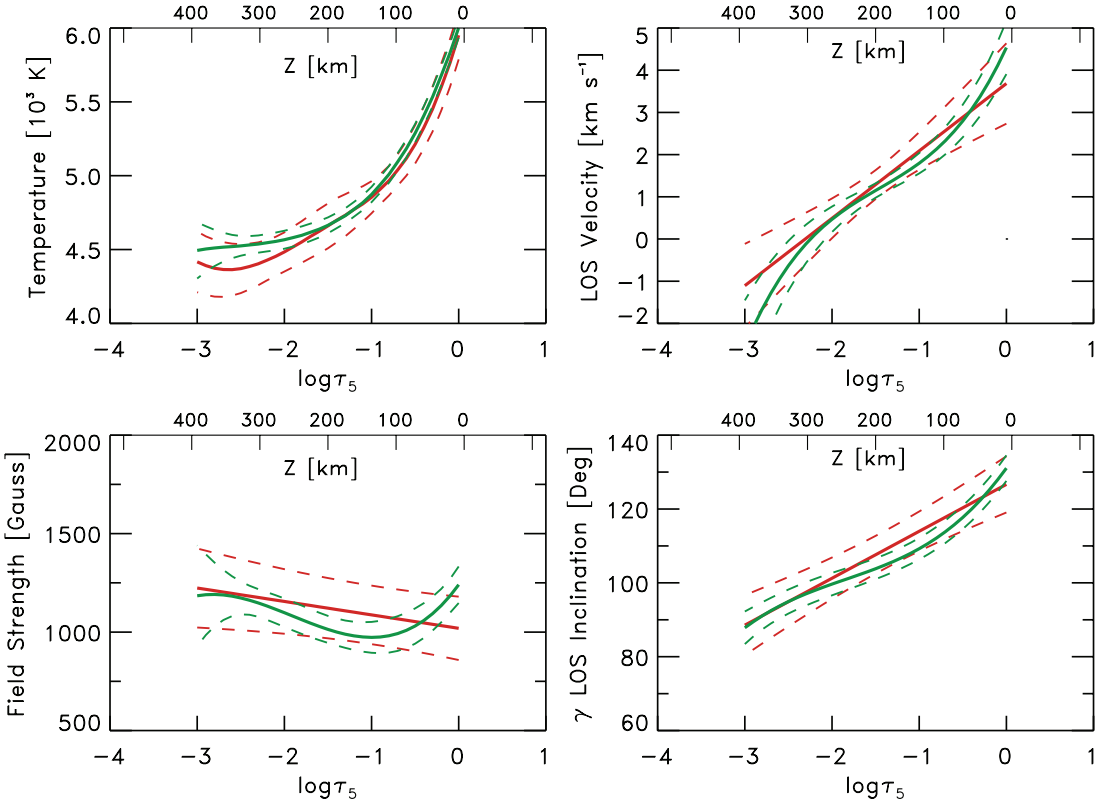

FIG. 6.—Temperature (*top left*), line-of-sight velocity (*top right*), magnetic field strength (*lower left*), and magnetic field inclination (*lower right*) as a function of the optical depth. Red indicates the average stratification obtained from the individual two-node inversion of the 2549 profiles belonging to family 1: $dB/d\tau < 0$ (taken from Fig. 3). Green shows the average stratification obtained from the individual four-node inversion of the Stokes vector of the same pixels.

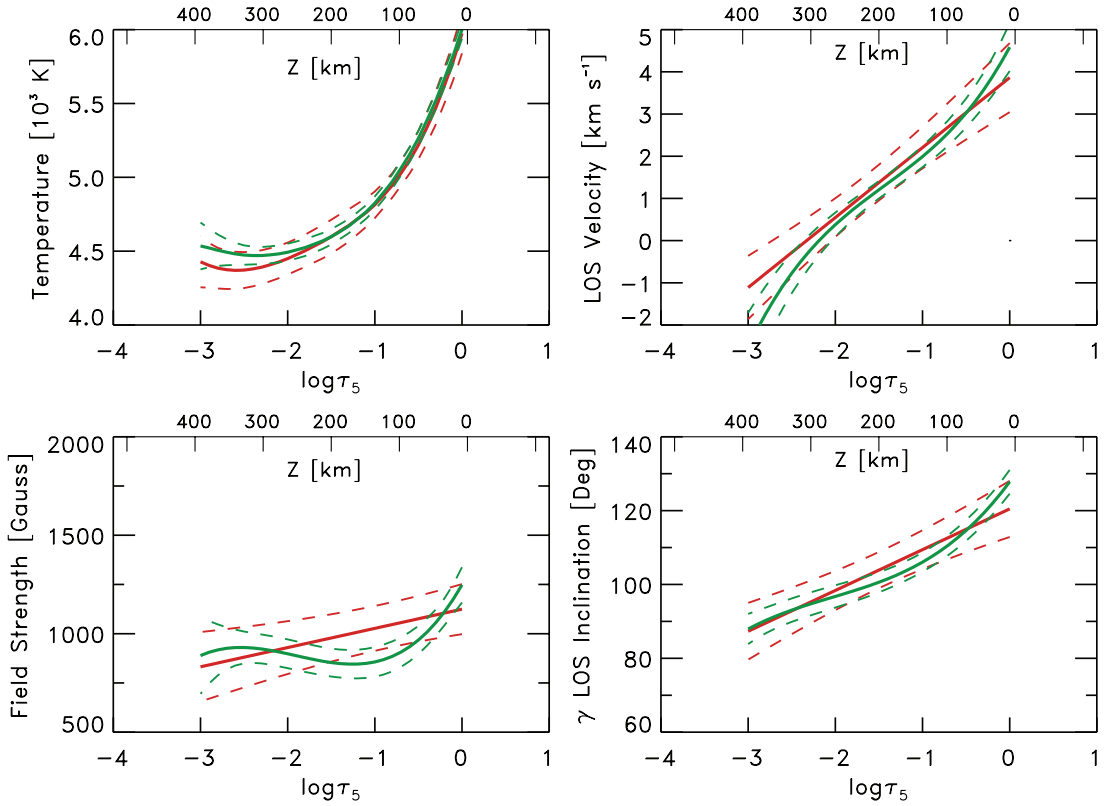

FIG. 7.—Same as Fig. 6, but for the 4971 pixels belonging to family 2: $dB/d\tau > 0$.

field as compared to the magnetic field high above it: $B_{\rm surr}$ versus $B_{\rm tube}$. A magnetic field that decreases smoothly toward the interior of the photosphere can be explained by a flux tube (of any field strength) whose upper boundary layer lies below $\tau_5 = 1$. If the upper boundary is above $\tau_5 = 1$, it can also be explained with a magnetic field inside the flux tube that is weaker than the magnetic field a few hundred kilometers above (solid lines plus filled circles in Fig. 8). In addition, a magnetic field that increases toward the interior of the photosphere is compatible with a flux tube

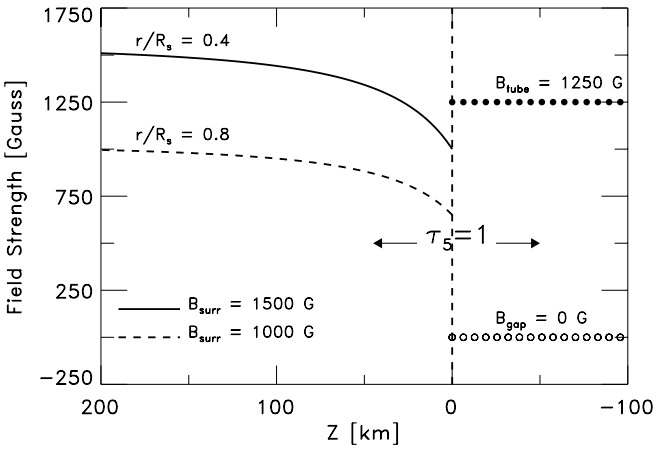

FIG. 8.—Vertical variation of the magnetic field strength across the center of a field-free gap (*open circles*) according to the gappy penumbral model. Same for a flux tube with a magnetic field strength of 1250 G (*filled circles*). Note that both models share the same stratification above the tube's or gap's boundary ($z > 0$). The solid line represents a situation where the external field is rather strong (*inner penumbra*), while the dashed line corresponds to the outer penumbra (*weak external field*). Also, note that the $\tau_5 = 1$ level can be shifted horizontally such that the continuum level can be formed above the gap/flux tube or inside them.

with an upper boundary layer above $\tau_5 = 1$, and with a stronger magnetic field than the one above (dashed line and filled circles in Fig. 8).

A more complex (four-node) inversion of intraspinal profiles indicates that, what appeared as two different families of structures using a two-node inversion, are likely to correspond to one single kind of magnetic structure, where the magnetic field exhibits an initial decrease between $\log \tau_5 \in [-3, -1.0]$, but increases between $\log \tau_5 \in [-1.0, 0]$ (see Figs. 6–7). While the gappy model offers no explanation for this effect, it can indeed be explained by the uncombed penumbral model, by means of a magnetic field whose strength decreases initially but increases once the line of sight crosses the flux tube's boundary (see Fig. 8). Furthermore, although intraspinal families 1 and 2 appear to be the equivalent in the four-node inversion, they still present a subtle yet important difference: family 1 (more commonly found in the inner penumbra; see Fig. 4) displays a much stronger initial decrease as compared to family 2, which is usually found in the outer penumbra (cf. lower left panels in Figs. 6 and 7).

This can be explained, in terms of the uncombed model if, at small and intermediate radial distances, the horizontal flux tube possesses a weaker magnetic field than the field in the atmosphere in which it is embedded: $B_{\rm tube} < B_{\rm surr}$ at r/R_s small (cf. solid line plus filled circles in Fig. 8 with green solid line in Fig. 6). As we move toward larger radial distances, and assuming that the magnetic field inside the flux tube remains constant, the surrounding magnetic field weakens and falls below the flux tube's field strength: $B_{\rm tube} > B_{\rm surr}$ at r/R_s large (cf. dashed line plus filled circles in Fig. 8 with solid green line in Fig. 7). Note that the assumption that the magnetic field in the flux tube remains constant is in agreement with a surrounding magnetic field whose strength decays much more rapidly toward the outer penumbra than inside the flux tube (see Fig. 4 in Borrero et al. [2004], Fig. 6 in Borrero

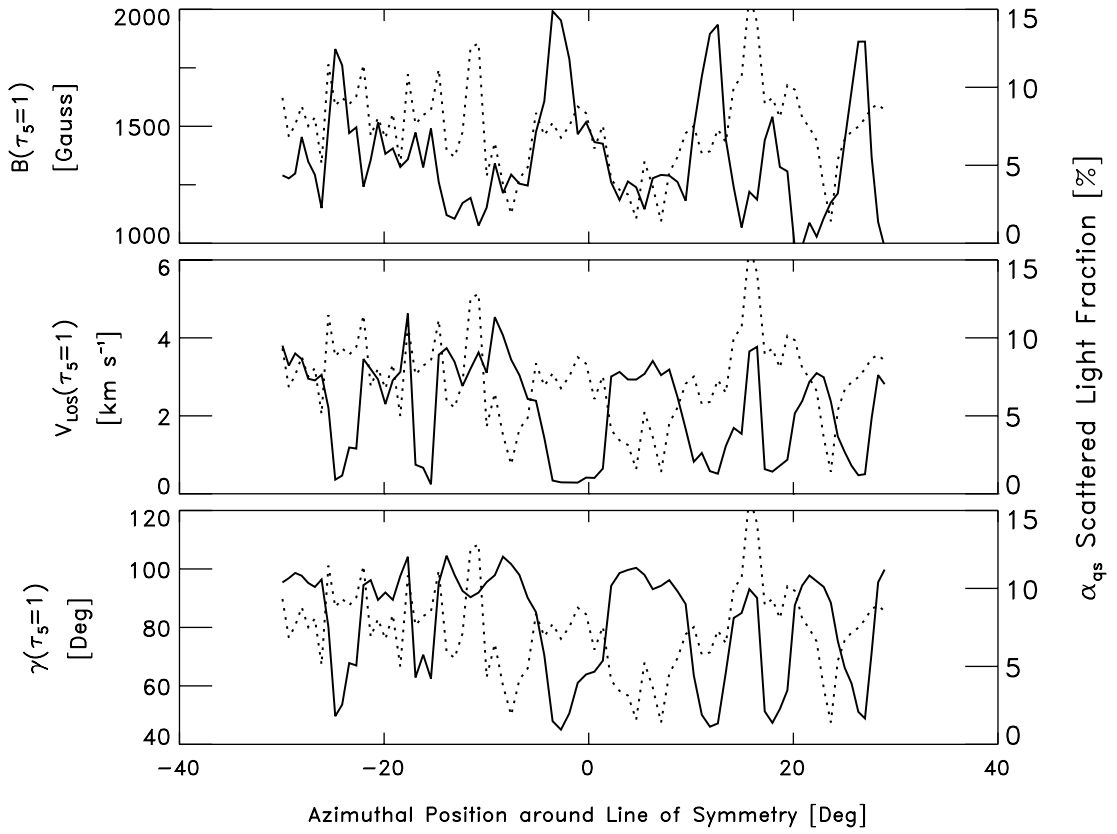

FIG. 9.—Azimuthal variation of the magnetic field strength (*top*), line-of-sight velocity (*middle*), and inclination of the magnetic field (*bottom*) at $\tau_5 = 1$, for a cut at a radial distance $r/R_s = 0.75$ in Fig. 2. The origin of the azimuth angle (*abscissa*) corresponds to the line of symmetry of the sunspot, indicated by the arrow in Fig. 1. The scattered light filling factor, α_{qs}, is also plotted in all three panels (*dashed lines*).

et al. [2005], and Fig. 4 in Borrero et al. [2006]). Here we find that this known feature of the penumbral intraspines helps to explain, within the frame of the uncombed model, differences in the stratification in the magnetic field strength across instrapines at different radial distances, as deduced from high-resolution spectropolarimetric observations.

5. SCATTERED LIGHT CONSIDERATIONS

One of the most critical issues in the inversion of spectropolarimetric data is the treatment of the scattered light. In order to properly model its contribution, detailed measurements of the telescope's point-spread function are needed. Since these are not usually available, the scattered light is often treated as a nonpolarized contribution to the total observed light (see § 3). In our study this is particularly important because one of the models under study (gappy model) postulates the existence of field-free regions around the $\tau_5 = 1$ level in the penumbra. These regions will naturally produce a nonpolarized contribution to the total observed Stokes vector. Therefore, there is a potential risk of not detecting the field-free gaps due to an incorrect treatment of the scattered light.

If our inversions are affected by this degeneracy between scattered light and field-free gaps, it is expected that those pixels where the intraspines are located show larger values for the amount of scattered light retrieved by the inversion (α_{qs}). To study this possibility we have plotted in Figure 9 the variations of the magnetic field strength (*top panel*), line-of-sight velocity (*middle panel*), and inclination angle (*bottom panel*) along an azimuthal cut at $r/R_s = 0.75$. Other azimuthal cuts at different radial distances show very similar behaviors. The values are taken at an optical depth of $\tau_5 = 1$ from the two-node inversion in § 3.2. This plot includes not only those pixels selected in Figure 2 as intraspines, but all of them. Therefore, regions where the magnitude of Evershed flow is reduced and the magnetic field is more vertical and strong (penumbral spines) are also visible. All three panels also show the amount of scattered light α_{qs} (*dashed lines*). There is no particular correlation between the location of penumbral intraspines (high velocities, weak and very inclined fields) and the regions where α_{qs} is largest. Similar variations are observed if we plot the values of the magnetic field strength and inclination, and line-of-sight velocity, at an optical depth of $\tau_5 = 10^{-2}$. This rules out the possibility that our inversions do not show field-free regions, in the deep photospheric layers, where intraspines are located at the expense of an enhanced scattered light contribution.

Recently, Orozco Suárez et al. (2007a, 2007b) have presented inversions of Stokes spectra measured using *Hinode*'s spectropolarimeter in the quiet Sun. These authors claim that for this instrument it is more appropriate to consider a local (unpolarized) scattered light profile. This is obtained by averaging the observed Stokes *I* profiles over a small region (about 1″) around the pixel that is being studied. In this case, a different scattered light profile is used in the inversion of each pixel. This approach can be justified by the fact that the focus of the Narrowband Filter Imager (NFI) on *Hinode* is favored when simultaneous observations are carried out with both instruments. In our inversions, we have, however, used a global scattered light profile, where we average the Stokes *I* signal emerging from the quiet-Sun region far away from the sunspot. In order to test whether our results depend on the use of a different scattered light profile, we have repeated our two-node inversion using the same approach as

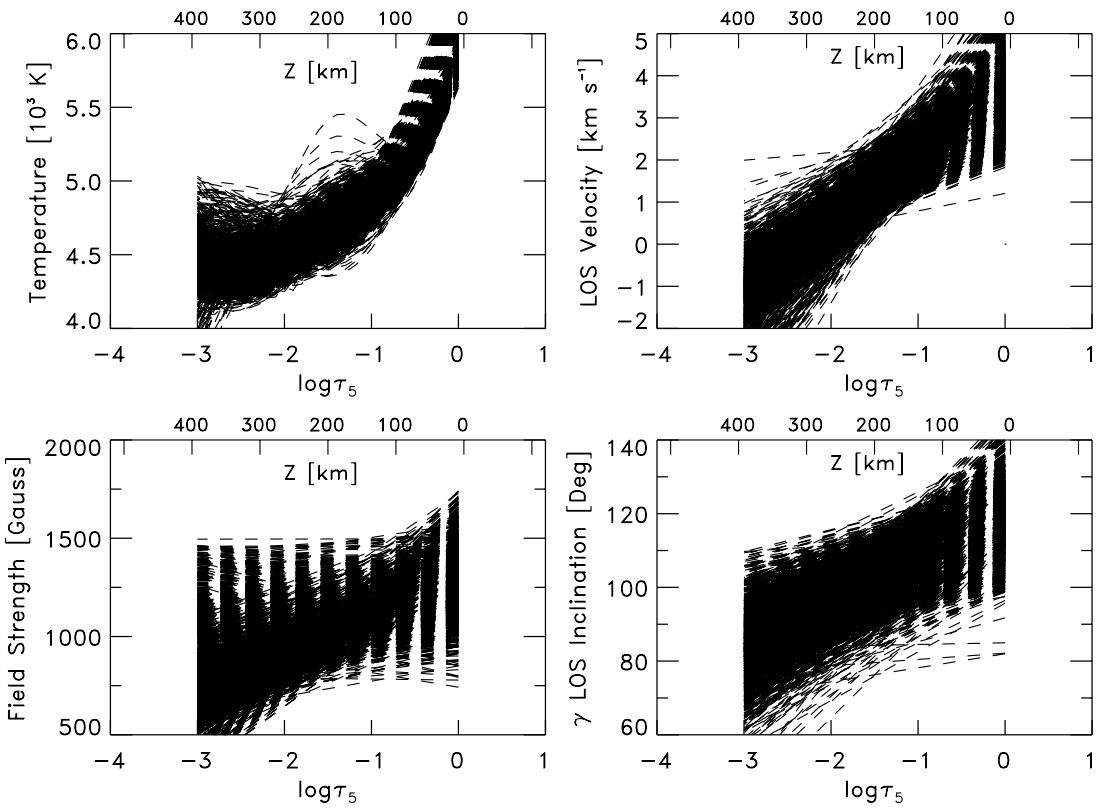

FIG. 10.—Same as Fig. 3, but using a *local* scattered light profile. About 90% of the inverted pixels show $dB/d\tau > 0$.

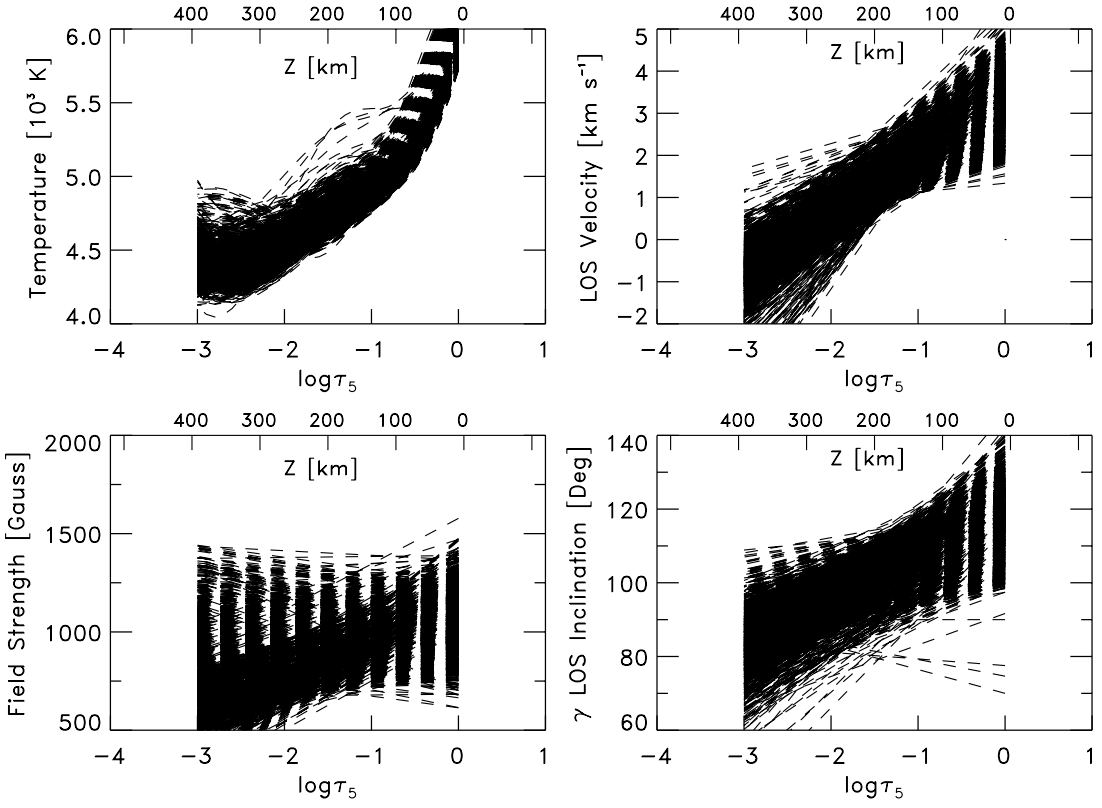

FIG. 11.—Same as Fig. 3, but *without* the scattered light. About 68% of the inverted pixels show $dB/d\tau > 0$.

Orozco Suárez et al. The results are presented in Figure 10 (cf. Fig. 3). The percentage of intraspinal pixels with $dB/d\tau > 0$ is even larger than before (90%).

Alternatively, Orozco Suárez et al. (2007a, 2007b) point out that the most realistic way to account for the scattered light would be to consider a local *and* polarized scattered light profile, where not only Stokes I is averaged, but also Stokes Q, U, and V. We have also tested this possibility. Unfortunately, this yields unrealistically high values for α_{qs} during the inversion: $\alpha_{qs} > 0.9$. This indicates that the inversion code tries to dominantly reproduce the observed Stokes profiles using the scattered light contribution. This is not surprising, since the neighboring Stokes profiles often look very similar to those in the pixel under study. Therefore, we conclude that this is not a reasonable approach when inverting sunspot data. We cannot rule out, however, that this treatment will work in quiet-Sun regions.

As a final test, we have repeated our two-node inversion, but neglecting any scattered light: $\alpha_{qs} = 0$. This test is very appropriate because, according to Spruit & Scharmer (2006), inversions of spectropolarimetric data fail to detect field-free regions in the penumbra as a consequence of these being already included in the scattered light profile. If their hypothesis is correct, not accounting for the scattered light contribution should uncover these regions with $B \simeq 0$ near $\tau_5 = 1$. Results ignoring the effects of the scattered light (Fig. 11) are essentially unchanged if compared to those where we used a global (Fig. 3) or local (Fig. 10) scattered light profile, with 68% of the pixels showing $dB/d\tau > 0$. The only difference is the increased temperatures obtained when we impose $\alpha_{qs} = 0$. In particular we do not see any pixel where the magnetic field reaches very small values in the deepest photospheric layers.

Taking into account all tests carried out in this section, it seems unlikely that the scattered light can significantly bias our magnetic field stratifications, consequently making it highly unlikely that we are missing the detection of field-free regions near $\tau_5 = 1$.

6. CONCLUSIONS

The *uncombed* model postulates that penumbral intraspines are characterized by the presence of horizontal flux tubes embedded in a surrounding atmosphere that possesses an inclined magnetic field. According to this model, looking along these regions should reveal a magnetic field that smoothly decreases at first, but once the flux tube contribution starts, the field strength could either increase or decrease. Alternatively, the *gappy* penumbral model postulates that instraspines correspond instead to regions where convective field-free gaps penetrate the penumbral field. In this case the magnetic field strength should also decrease with optical depth at first, but suffer a much larger drop once the line of sight crosses the field-free gap.

In order to differentiate between these two models, we have used polarimetric data at very high spatial resolution, recorded with the spectropolarimeter on board the Japanese spacecraft *Hinode*, to investigate the depth variation of the magnetic field strength in the penumbra. We have selected a large number ($\sim$7500) of pixels that are representative of weak and horizontal magnetic fields (i.e., penumbral intraspines) carrying strong Evershed flows. From the inversion of the Stokes profiles at these locations we find that the magnetic field strength can either increase or decrease with optical depth. A more detailed inversion of the average Stokes vector over the selected pixels shows that the magnetic field initially decreases, between $\log \tau_5 \in [-3, -0.7]$, but increases thereafter until $\log \tau_5 = 0$.

The gappy penumbral model can explain a smoothly decreasing magnetic field strength only if the $\tau_5 = 1$ level is formed above the field free gap; otherwise, a much more sudden decrease would be observed as the line of sight penetrates the field-free plasma. A partial solution to this problem can be found if we assume that the gap is not fully evacuated of magnetic field. However, it offers no explanation for about 66% of the selected pixels, where an increasing magnetic field strength with optical depth is observed. The absence of field-free gaps, as indicated by the inversion, does not in itself imply that there is no form of convection present in the penumbra, but rather suggests that the convective energy transport takes places in the presence of a magnetic field (see Zakharov et al. 2008; Rempel et al. 2008). An example is the roll convection proposed by Danielson (1961).

All inferred stratifications are compatible with the scenario proposed by the uncombed model. A magnetic field that decreases smoothly toward the interior of the photosphere can be explained by either a flux tube (of any field strength) whose upper boundary layer lies below $\tau_5 = 1$ or, if the upper boundary is above $\tau_5 = 1$, with a magnetic field inside the flux tube that is weaker than the magnetic field a few hundred kilometers above. In addition, a magnetic field that increases toward the interior of the photosphere is compatible with a flux tube with an upper boundary layer above $\tau_5 = 1$, but with a stronger magnetic field than the one above. This very same configuration can explain a magnetic field that first decreases and then increases with optical depth, as inferred from the inversion of averaged intraspinal profiles.

We have also studied the effects of the scattered light in our inversions. We have seen that any inaccuracies in its treatment are unlikely to be a source of error in the stratification of the magnetic field strength. It would be very desirable to make a robust confirmation of our findings, namely $dB/d\tau > 0$ in the outer penumbra, for a larger number of sunspots at different heliocentric angles and including also the diskward side of the penumbra. A natural extension of this work would be to use the Fe I lines at 1.56 μm (which are formed deeper in the photosphere) to confirm the absence of field-free regions around $\tau_5 = 1$. Unfortunately, no such observations exist at the spatial resolution needed to resolve penumbral intraspines ($\simeq 0.4''$). Indeed, some studies at slightly lower resolution ($0.6''$–$0.7''$) have been presented by Cabrera Solana et al. (2008), who used simultaneous observations of Fe I 630 nm and 1.56 μm recorded with the TIP (Martínez Pillet et al. 1999) and POLIS (Schmidt et al. 2003) instruments. They found that in the outer penumbra, the horizontal magnetic field component (carrying the Evershed flow) was no longer weaker than the more vertical one. This can be used as an independent confirmation of our work, where we routinely find $dB/d\tau > 0$ at large radial distances from the center of the sunspot. In addition, flux tubes with stronger magnetic field than that of the environment in which they are embedded are also necessary to explain certain aspects of the net circular polarization observed in the outer penumbra of sunspots (Tritschler et al. 2007; Ichimoto et al. 2008).

REFERENCES

Bello González, N., Okunev, O. V., Domíguez Cerdeña, I., Kneer, F., & Puschmann, K. G. 2005, A&A, 434, 317
Bellot Rubio, L. R. 2003, in ASP Conf. Ser. 307, Solar Polarization, ed. J. Trujillo & J. Sánchez Almeida (San Francisco: ASP), 301
Bellot Rubio, L. R., Baltasar, H., & Collados, M. 2004, A&A, 427, 319
Borrero, J. M. 2007, A&A, 471, 967
Borrero, J. M., Lagg, A., Solanki, S. K., & Collados, M. 2005, A&A, 436, 333
Borrero, J. M., Lites, B. W., & Solanki, S. K. 2008, A&A, 481, L13
Borrero, J. M., Solanki, S. K., Bellot Rubio, L. R., Lagg, A., & Mathew, S. K. 2004, A&A, 422, 1093

Borrero, J. M., Solanki, S. K., Lagg, A., Socas-Navarro, H., & Lites, B. W. 2006, A&A, 450, 383
Cabrera Solana, D., Bellot Rubio, L. R., Borrero, J. M., & Del Toro Iniesta, J. C. 2008, A&A, 477, 273
Danielson, R. E. 1961, ApJ, 134, 289
Del Toro Iniesta, J. C. 2003, Introduction to Spectropolarimetry (Cambridge: Cambridge Univ. Press)
Ichimoto, K., et al. 2008, A&A, 481, L9
Kosugi, T., et al. 2007, Sol. Phys., 243, 3
Langhans, K., Scharmer, G., Kiselman, D., Löfdahl, M. G., & Berger, T. E. 2005, A&A, 436, 1087
Lites, B. W., Elmore, D. F., Seagraves, P., & Skumanich, A. P. 1993, ApJ, 418, 928
Lites, Q. W., Elmore, D. F., & Streander, K. V. 2001, in ASP Conf. Ser. 236, Advanced Solar Polarimetry, ed. M. Sigwarth (San Francisco: ASP), 33
Martínez Pillet, V. 2000, A&A, 361, 734
Martínez Pillet, V., et al. 1999, in ASP Conf. Ser. 183, High Resolution Solar Physics: Theory, Observations, and Techniques, ed. T. R. Rimmele, K. S. Balasubramanian, & R. R. Radick (San Francisco: ASP), 264
Mathew, S. K., et al. 2003, A&A, 410, 695
Orozco Suárez, D., Bellot Rubio, L. R., & Del Toro Iniesta, J. C. 2007a, ApJ, 662, L31
Orozco Suárez, D., et al. 2007b, ApJ, 670, L61
Rempel, M., Schussler, M., & Knolker, M. 2008, ApJ, submitted (arXiv: 0808.3294v1)
Rüedi, I., Solanki, S. K., Keller, C. U., & Frutiger, C. 1998, A&A, 338, 1089
Ruiz Cobo, B., & Del Toro Iniesta, J. C. 1992, ApJ, 398, 375
Scharmer, G. B., Gudiksen, B. V., Kiselman, D., Löfdahl, M. G., & Rouppe van der Voort, L. H. M. 2002, Nature, 420, 151
Scharmer, G., & Spruit, H. C. 2006, A&A, 460, 605
Schlichenmaier, R., Jahn, K., & Schmidt, H. U. 1998, A&A, 337, 897
Schmidt, W., Beck, C., Kentischer, T., Elmore, D., & Lites, B. W. 2003, Astron. Nachr., 324, 300
Shimizu, T., et al. 2008, Sol. Phys., 249, 221
Solanki, S. K. 2003, A&A Rev., 11, 153
Solanki, S. K., & Montavon, C. A. P. 1993, A&A, 275, 283
Spruit, H. C., & Scharmer, G. B. 2006, A&A, 447, 343
Stanchfield, D. C. H., II, Thomas, J. H., & Lites, B. W. 1997, ApJ, 477, 485
Tritschler, A., Müller, D. A. N., Schlichenmaier, R., & Hagenaar, H. J. 2007, ApJ, 671, L85
Westendorp Plaza, C., Del Toro Iniesta, J. C., Ruiz Cobo, B., Martínez Pillet, V., Lites, B. W., & Skumanich, A. 1998, ApJ, 494, 453
———. 2001, ApJ, 547, 1130
Zakharov, V., Hirzberger, J., Riethmueller, T., Solanki, S. K., & Kobel, P. 2008, A&A, 488, L17